J Mater Sci (2014) 49:5961–5977
DOI 10.1007/s10853-014-8315-z

Impurity effects on the nucleation and growth of primary $Al_3(Sc,Zr)$ phase in Al alloys

J. H. Li · B. Oberdorfer · S. Wurster · P. Schumacher

Received: 3 February 2014 / Accepted: 8 May 2014 / Published online: 22 May 2014

Abstract Impurity effects on the nucleation and growth of primary $Al_3(Sc,Zr)$ phase have been investigated in high purity Al alloys and commercial purity Al alloys, respectively. In the case of high purity Al alloys, primary $Al_3(Sc,Zr)$ phases were found to be pushed to grain boundaries ahead of the solidification front. Such type of primary $Al_3(Sc,Zr)$ phase did not contribute to the heterogeneous nucleation, and thereby the grain refinement of Al alloys. In the case of commercial purity Al alloys, the presence of Fe, Si, Cu, Mg, Ti, and other impurities significantly enhanced the heterogeneous nucleation of primary $Al_3(Sc,Zr)$ phase. Most primary $Al_3(Sc,Zr)$ phases were found to be located within the α-Al matrix, and kept an identical orientation relationship with the α-Al matrix. Furthermore, the presence of the impurities also changed the growth mode on the primary $Al_3(Sc,Zr)$ phase. In the case of commercial purity Al alloys, a peritectic to eutectic reaction was induced due to the presence of the impurities. A layered growth was observed leading to a narrow particle size distribution. In contrast, in the case of high purity Al alloys, a featureless structure was observed. This investigation demonstrates that impurities and their concentrations are important factors affecting the nucleation and growth of primary $Al_3(Sc,Zr)$ phases, and thereby for the successful grain refinement in Al-based alloys.

Electronic supplementary material The online version of this article (doi:10.1007/s10853-014-8315-z) contains supplementary material, which is available to authorized users.

J. H. Li (✉) · P. Schumacher
Institute of Casting Research, University of Leoben, 8700 Leoben, Austria
e-mail: jie-hua.li@hotmail.com

B. Oberdorfer · P. Schumacher
Austrian Foundry Research Institute, 8700 Leoben, Austria

S. Wurster
Department of Materials Physics, Erich Schmid Institute of Materials Science of the Austrian Academy of Sciences, University of Leoben, 8700 Leoben, Austria

Introduction

Grain refinement of Al alloys has been extensively investigated for several decades both in industry and academic, not only for developing efficient grain refiners, but also for achieving a better understanding of the grain refinement mechanisms [1–13]. During grain refinement of Al alloys, Al–Ti–B grain refiners have been widely investigated, due to their high nucleation potency and wide industrial application. Various theories regarding the grain refinement mechanisms of Al–Ti–B refiners, such as the particle theory, the phase diagram theory, the duplet nucleation theory, and the peritectic bulk theory, have been proposed and reviewed in [1]. Recently, free growth theory [2–6], modified free growth theory [7],and interdependence theory [8] have also been proposed. Despite the differences between these theories, it is generally accepted that the impurity of Ti has a dual role within the melt. One role is to create an enriched Ti region leading to the formation of an Al_3Ti monolayer necessary for the nucleation of Al on the stable boride substrates (TiB_2) [10–13]. The other role is to act as an effective growth restrictor [1, 5, 8], which is proportional to the initial rate of constitutional undercooling development and can be used directly as a criterion of the grain refinement in Al alloys with strong potential nucleating particles. The combined effects of enhanced copious potent nuclei and growth restriction result in the

formation of desirable, small uniform equiaxed Al grains. If the excess Ti is regarded as a trace impurity, it is clear that there is an important impurity effect on the nucleation (Al_3Ti monolayer on TiB_2) and growth (growth restriction) of Al alloys.

Even smaller grain sizes than with Al–Ti–B grain refiner addition can be obtained with hypoeutectic addition of Sc and/or Zr into Al-based alloy. Interestingly, both Zr and Sc only exhibit a small growth restriction in Al alloys. Thus, the grain refinement effect may be mainly dominated by heterogeneous nucleation. In the early 1960s, the potential of Sc in controlling microstructure of Al-based alloys has been recognized [14, 15]. The grain refinement occurred in hypereutectic compositions and was shown to be far greater than that can be achieved by conventional Al grain refiners. Furthermore, grain refinement by Sc addition was found to be accompanied by a change in growth morphology from unrefined dendritic, to fine spherical grains with a divorced eutectic appearing on the grain boundaries in the refined castings [16].

In order to further decrease the expensive Sc addition, a combined addition of Zr and Sc was found to enable a considerable grain refinement in Al alloys, which is much stronger than that of Zr or Sc alone. Significant improvements in properties of commercial 2×××, 5×××, 7××× have been achieved through Sc and Zr additions [14]. However, most previous research focus on the decomposition of supersaturated Al–Sc solid solutions, which leads to the formation of the fully coherent, secondary $L1_2$_$Al_3(Sc,Zr)$ phase [17–24]. As a consequence, $Al_3(Sc,Zr)$ precipitates are extremely fine, homogeneously distributed (typically <20 nm), with number densities approaching those observed for GP zones.

An important impurity effect on the precipitation in dilute Al–Sc-based alloys has been reported in [19–21]. The presence of Si in commercial purity Al alloys has been reported to increases the Al_3Sc precipitation kinetics, and increases the number density in solids. This acceleration has been attributed to the facts that (i) Si partitions preferentially to the Al_3Sc precipitates occupying the Al sublattice site, (ii) Si increases the driving force for the precipitation of Al_3Sc, and (iii) Si partitions preferentially to Al_3Sc ($L1_2$) rather than Al_3Zr ($L1_2$). Furthermore, Ti was also found to be incorporated into the $Al_3(Sc,Ti)$ precipitates (L12 structure), whose Ti content increases with increasing aging time and temperature, especially at the interface where Ti segregates. The significantly smaller diffusivity of Ti in Al compared to that of Sc in Al has been used to interpret the exceptional coarsening resistance of $Al_3(Sc,Ti)$ precipitates [23]. With the small Ti addition (0.04 wt% Ti), the decomposition sequence of Al-0.22Sc-0.13Zr (wt%) alloy and the formation of a layer enriched in Ti in the solid state was observed as: Sc-rich clusters → Al_3Sc phase → layer enriched in Zr → layer enriched in Ti → $Al_3(Sc,Zr,Ti)$ phase [24]. The influence of the Si (0.04 at.%) and Er (0.01 at.%) addition on the coarsening of the $Al_3(Sc,Zr)$ particles in Al-0.06Zr-0.06Sc (at.%) alloy has been reported in the solid state [21]. Clearly, the presence of impurities (e.g., Si, Ti) has a great effect on precipitation kinetics of secondary $Al_3(Sc,Zr)$ phase in dilute Al–Sc alloys. However, much less attentions have been paid to the primary $Al_3(Sc,Zr)$ phase directly solidified from liquid. The presence of such type of the impurities can also be expected to affect the nucleation and growth of primary $Al_3(Sc,Zr)$ phase, enhancing the heterogeneous nucleation of α-Al during solidification. However, there is still a lack of detailed investigations on the nucleation and growth of primary $Al_3(Sc,Zr)$ phase.

In this paper, the nucleation and growth of primary $Al_3(Sc,Zr)$ phase has been investigated in high purity Al alloys and commercial purity Al alloys, with a special focus on the impurity effects. The nucleation and growth modes are also discussed.

Table 1 The nominal composition of Zr and Sc in high purity Al alloys and commercial purity Al alloys with Zr and/or Sc additions

Alloy no.	Zr	Sc	Al
1	–	–	Bal.
2	0.1 (0.08)	–	Bal.
3	0.2 (0.22)	–	Bal.
4	0.5 (0.46)	–	Bal.
5	–	0.1 (0.8)	Bal.
6	–	0.2 (0.15)	Bal.
7	–	0.5 (0.43)	Bal.
8	0.05 (0.04)	0.05 (0.045)	Bal.
9	0.1 (0.11)	0.1 (0.08)	Bal.
10	0.25 (0.24)	0.25 (0.23)	Bal.
11	–	–	Bal.
12	0.1 (0.09)	–	Bal.
13	0.2 (0.18)	–	Bal.
14	0.5 (0.47)	–	Bal.
15	–	0.1 (0.092)	Bal.
16	–	0.2 (0.14)	Bal.
17	–	0.5 (0.42)	Bal.
18	0.05 (0.06)	0.05 (0.047)	Bal.
19	0.1 (0.12)	0.1 (0.077)	Bal.
20	0.25 (0.27)	0.25 (0.21)	Bal.

The composition of Zr and Sc were measured using ICP and given in brackets (wt%). The compositions of Si, Fe, Mg, Cu, Ti, and other impurities were taken from the measured results of the high purity Al and commercial purity Al, respectively. In high purity Al (alloys 1–10), Si (7 ppm), Fe (6 ppm), Cu (8 ppm), Mg (4 ppm), and Ti (<1 ppm) was measured While, in commercial purity Al (alloys 11–20), Si (0.0675), Fe (0.805), Cu (0.0011), Mg (0.0113), and Ti (0.0117) was measured

Experimental material and procedures

A series of high purity Al-based alloys with Zr and/or Sc additions were prepared using high purity Al ingots (5N, 99.998), Al-10 wt% Zr, and an Al-2.2 wt% Sc master alloys (wt%, used throughout the paper unless noted otherwise), respectively. For comparison, a series of commercial purity Al-based alloys with Zr and/or Sc additions were also prepared using commercial purity Al ingots (2N8, 99.8), Al-10Zr and an Al-2.2Sc master alloys, respectively. The nominal compositions are listed in Table 1. Furthermore, the compositions of Zr and Sc have been measured using inductively coupled plasma atomic emission spectroscopy (ICP-AES) and are given in brackets in Table 1. Some differences between the measured composition and nominal composition can be partly due to the measuring error (about 2–5 %) of the ICP-AES methods. It should be noted that in high purity Al (alloys 1–10), Si (7 ppm), Fe (6 ppm), Cu (8 ppm), Mg (4 ppm), and Ti (<1 ppm) was measured in high purity Al (5N). While, in commercial purity Al (alloys 11–20), Si (0.0675), Fe (0.805), Cu (0.0011), Mg (0.0113), and Ti (0.0117) was measured in commercial purity Al (2N8). Clearly, significant impurities (Si, Fe, Mg, and Ti) are present in commercial purity Al alloys.

Each batch, weighting about 6 kg, was melted in a resistance furnace at 720 °C. A reference sample was taken from the melt in order to identify the grain size before the additions of Al-10Zr and/or Al-2.2Sc master alloys. The melt was stirred with a graphite rod for 20 s after inoculation. The samples were taken from the melt after the addition of Al-10Zr and/or Al-2.2Sc master alloys (about 5 min) and tested using standard TP-1 test [2].

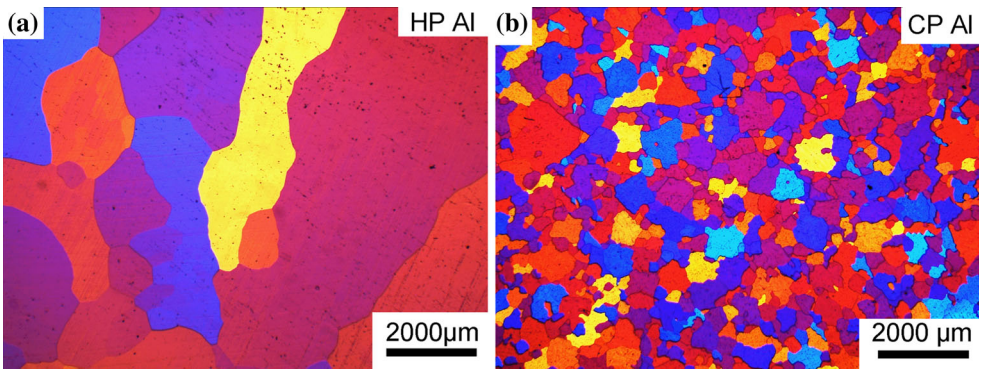

Fig. 1 Grain size of high purity Al alloy (**a**) and commercial purity Al alloy (**b**), respectively. Note that all images are taken from the TP-1 test (cooling rate: about 4 °C/s)

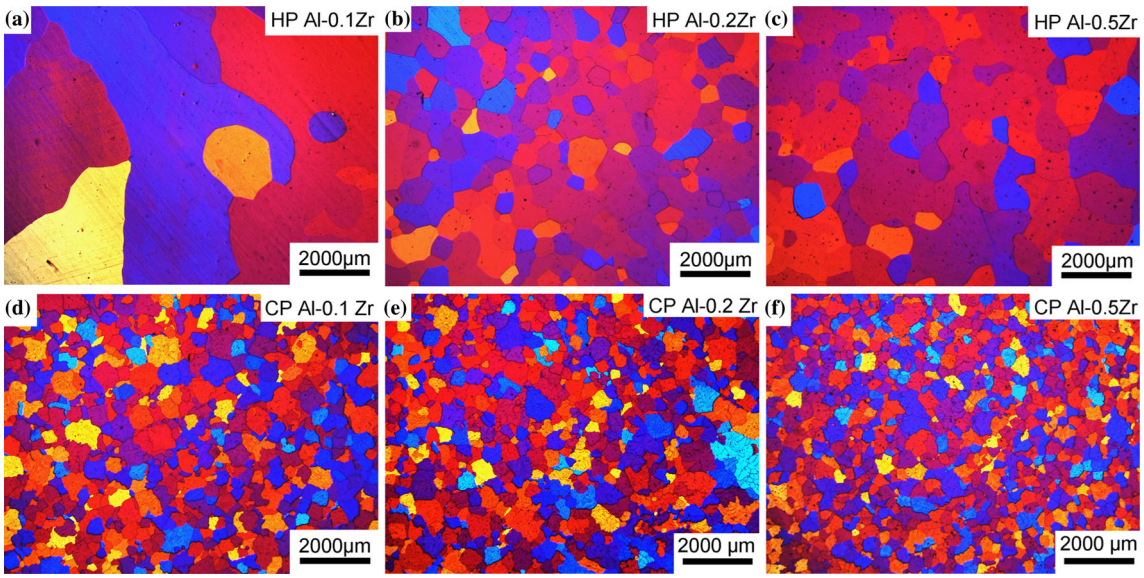

Fig. 2 Grain size of high purity Al alloy and commercial purity Al alloy with the additions of 0.1Zr (**a**, **d**), 0.2Zr (**b**, **e**), and 0.5Zr (**c**, **f**), respectively. Note that all images are taken from the TP-1 test (cooling rate: about 4 °C/s)

Table 2 Phase diagram data for determining growth restrictor factor in binary Al alloys [25]

Element	k	m	Max. conc. (wt%)	$m\ (k-1)$
Zr	2.5	4.5	0.11	6.8
Fe	0.02	−3.0	~1.8	2.9
Sc	0.64	−9.1	0.55	3.3
Ti	7–8	33.3	0.15	~220

According to the TP-1 test, the samples were sectioned 38 mm from the bottom surface. Standard metallographic procedures were performed to prepare these sections for grain size measurements. The samples were etched using a mixture of 13 g boric acid, 35 g HF, 800 ml H_2O at a voltage of 20 V for 45 s. All images used for grain size measurement were taken from the center of the samples using optical microscopy in a polarized mode. The reported grain sizes were measured from at least 20 images using the line-intersect method.

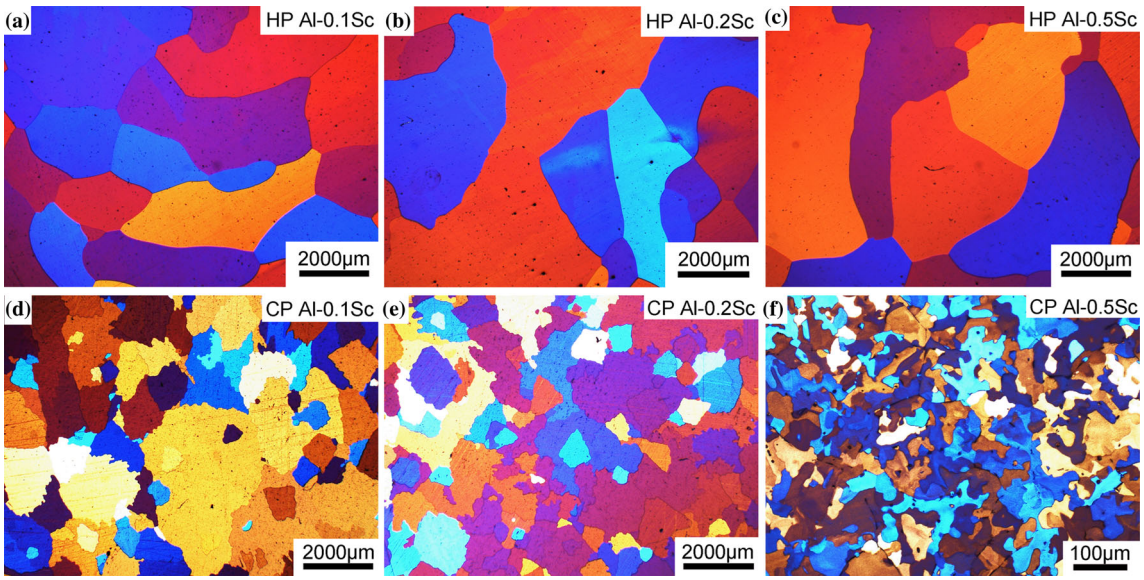

Fig. 3 Grain size of high purity Al alloy and commercial purity Al alloy with the additions of 0.1Sc (**a**, **d**), 0.2Sc (**b**, **e**), and 0.5Sc (**c**, **f**), respectively. Note that all images are taken from the TP-1 test (cooling rate: about 4 °C/s)

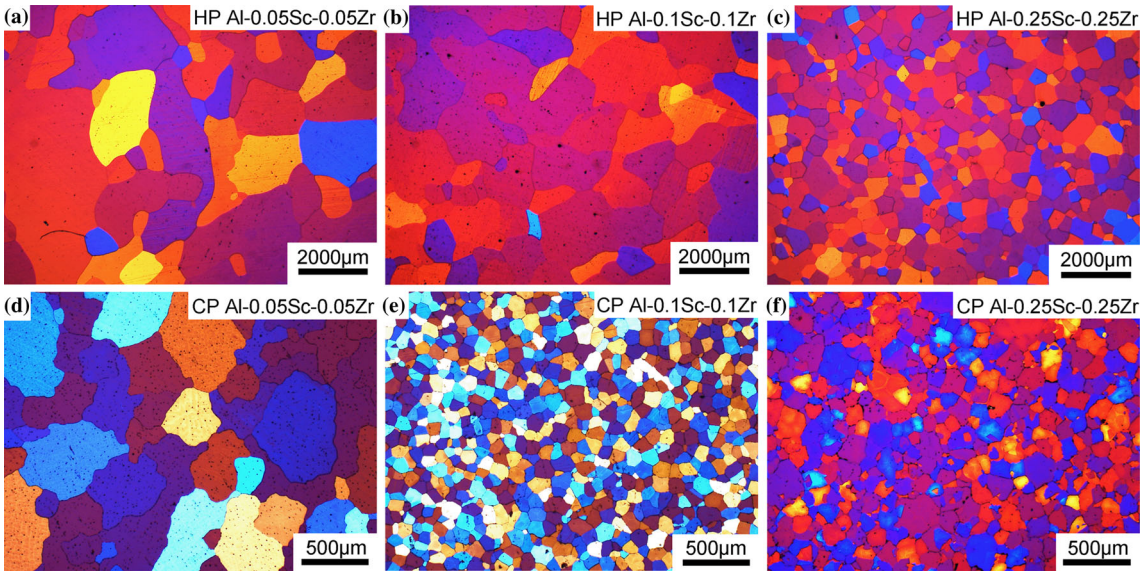

Fig. 4 Grain size of high purity Al alloy and commercial purity Al alloy with the additions of 0.05Sc and 0.05Zr (**a**, **d**), 0.1Sc and 0.1Zr (**b**, **e**), and 0.25Sc and 0.25Zr (**c**, **f**), respectively. Note that all images are taken from the TP-1 test (cooling rate: about 4 °C/s)

The samples for computed tomography (CT) investigations were machined to be 2.4-mm in diameter and 3-mm in length. In order to further check the distribution of primary Al_3(Sc,Zr) phases, a commercial purity Al-6Zn-2Mg alloy with 0.25Sc, 0.15Zr, and 0.01Ti additions was also used for CT investigation. The enhanced contrast caused by these alloying elements along the grain boundaries makes it possible to determinate the distribution of primary Al_3(Sc,Zr) phases. It should be noted here that the presence of 0.01Ti is from the commercial purity Al, rather than through Ti alloying.

The samples were scanned on a Phoenix X-ray v|tomexc equipped with a 240 kV cone-beam X-ray tube. At least 2000 X-ray images were recorded within a total scan time of about 340 min using a GE DXR 1000 × 1000 pixel detector with 14 bit dynamic range. For the volume reconstruction, a modified Feldkamp algorithm for the filtered back projection as implemented by the system supplier was used. The resulting voxel size was about 3.2 μm. Number density and the size distribution of Al_3(Sc,Zr) particle were thus determined in high purity Al-0.25Sc-0.25Zr alloy, commercial purity Al-0.25Sc-0.25Zr alloy, and commercial Al-6Zn-2Mg-0.25Sc-0.01Ti-0.15Zr alloy, respectively.

The samples for scanning electron microscopy (SEM) and electron backscatter diffraction (EBSD) investigation

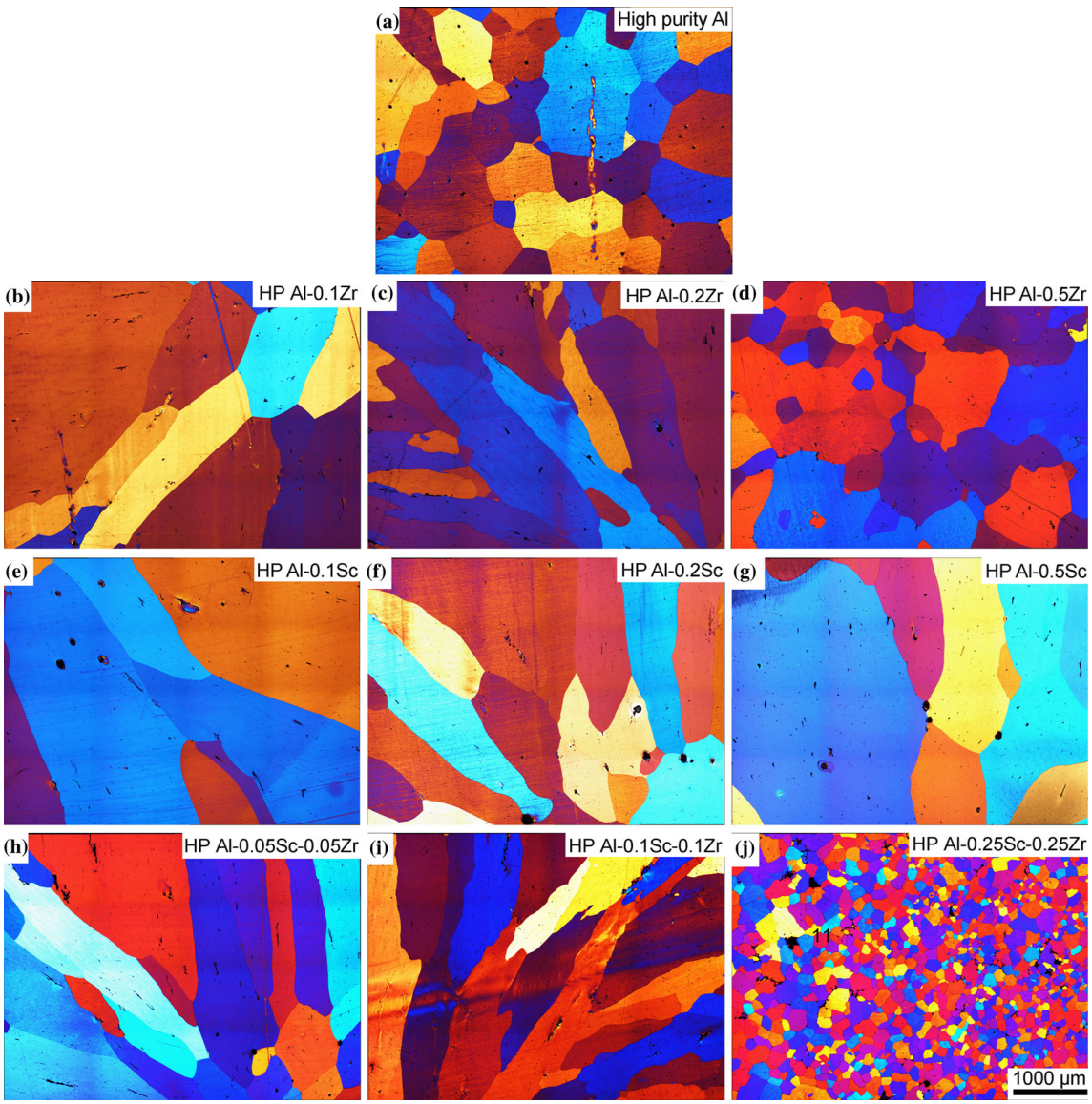

Fig. 5 Grain size of high purity Al (**a**) and high purity Al alloy with the additions of 0.1Zr (**b**), 0.2Zr (**c**), and 0.5Zr (**d**), 0.1Sc (**e**), 0.2Sc (**f**), 0.5Sc (**g**), 0.05Sc and 0.05Zr (**h**), 0.1Sc and 0.1Zr (**i**), 0.25Zr and 0.25Sc (**j**), respectively. Note that all images are taken from the thermal analysis samples (cooling rate: about 20 °C/min) at the same magnification, as marked in (**j**)

were mechanically ground and electron-polished in a solution consisted of 5 % perchloric acid and 95 % methanol at −30 °C. EBSD investigation was performed using a Zeiss 1525 scanning electron microscope equipped with an EDAX EBSD system. Evaluation of scans was made with orientation imaging microscopy (OIM) software. The EBSD investigation can be used to determine the orientation relationship between the primary $Al_3(Sc,Zr)$ particles and the α-Al matrix. However, the texture analysis is not the focus of the present paper because primary $Al_3(Sc,Zr)$ phase was solidified directly from the liquid, which is different from the precipitation of secondary $Al_3(Sc,Zr)$ phase from the solid state, in particular after severe deformation.

Results

As-cast microstructure of high purity and commercial purity Al alloy with the additions of Sc and/or Zr

Figure 1 shows typical as-cast microstructures of high purity and commercial purity Al alloys. In the case of high purity Al alloy, the grain size is very large, about 800 ± 50 μm (Fig. 1a). Most grains appear to be columnar. While, in the case of commercial purity Al, the grain size is much finer, about 270 ± 45 μm (Fig. 1b). Most grains appear to be equiaxed. The enhanced grain refinement and the columnar to equiaxed transformation (CET)

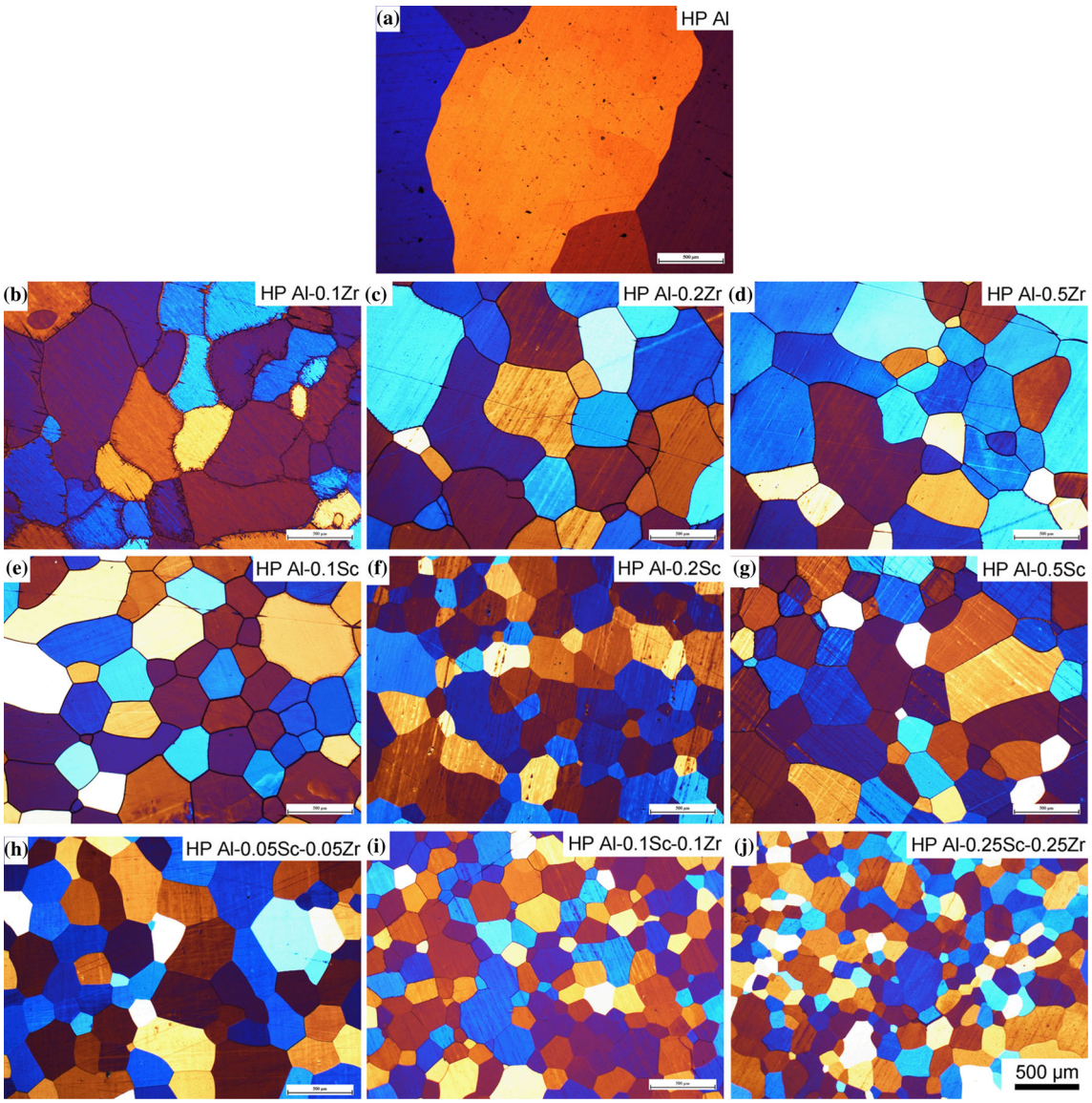

Fig. 6 Grain size of high purity Al (**a**) and high purity Al alloy with the additions of 0.1Zr (**b**), 0.2 Zr (**c**), and 0.5Zr (**d**), 0.1Sc (**e**), 0.2Sc (**f**), 0.5Sc (**g**), 0.05Sc and 0.05Zr (**h**), 0.1Sc and 0.1Zr (**i**), 0.25Zr and 0.25Sc (**j**), respectively. Note that all images are taken from the Spark analysis samples (cooling rate: about 20 °C/s) at the same magnification, as marked in (**j**)

indicate that impurities (e.g., Si, Fe, Cu, Mg, and Ti) have an important effect on the nucleation and growth of α-Al.

No significant grain refinement was observed in high purity Al alloys with the addition of 0.1Zr, as shown in Fig. 2a. Most grains appear to be still columnar. This observation is consistent with the fact that Zr has a maximum solubility (0.11 wt%) in Al (Table 2). In the case of 0.1Zr addition in high purity Al alloy, no significant Al_3Zr phase is formed, which could act as a nucleation site for the α-Al. Furthermore, no significant grain refinement can be provided as the growth restriction of Zr is low (6.8 K/wt%, Table 2). Increasing Zr addition up to 0.2 results into an enhanced grain refinement. With further increasing Zr addition from 0.2 to 0.5, no significant decrease of the grain size was observed, demonstrating that a further increase of Zr addition cannot enhance the grain refinement despite slightly increasing the growth restriction. In contrast, a smaller gain size was observed in commercial purity Al when compared with high purity Al with the same Zr addition (e.g., 0.1, 0.2, and 0.5). This enhanced grain refinement can be directly attributed to the impurity effect on the nucleation and growth, because all other experimental conditions remained unchanged.

An even stronger contrast was observed in the case of Sc addition into high purity Al and commercial purity Al, as shown in Fig. 3. No significant grain refinement was observed in high purity Al even with the addition of 0.5Sc, as shown in Fig. 3c. Most grains appear to be still columnar. This observation is also consistent with the fact that Sc has a higher maximum solubility (0.55 wt%) in Al (Table 2). In all cases of Sc additions in high purity Al, no significant number of primary Al_3Sc phase was formed as an effective nucleation site for α-Al, thus no significant grain refinement can be observed. Similar to the Zr addition in commercial purity Al, a smaller gain size was observed when compared with high purity Al with the same Sc addition (e.g., 0.1, 0.2, and 0.5). This enhanced grain refinement can be directly attributed to impurity effects.

An enhanced grain refinement was observed in high purity Al and commercial purity Al with the combined additions of Sc and Zr, as shown in Fig. 4. It should be noted that there is no great change of the total combined addition of Zr and Sc, when compared with the single addition of Zr (Fig. 2) or Sc (Fig. 3). In addition, the growth restriction of Sc (3.3 K/wt%, Table 2) in Al is two

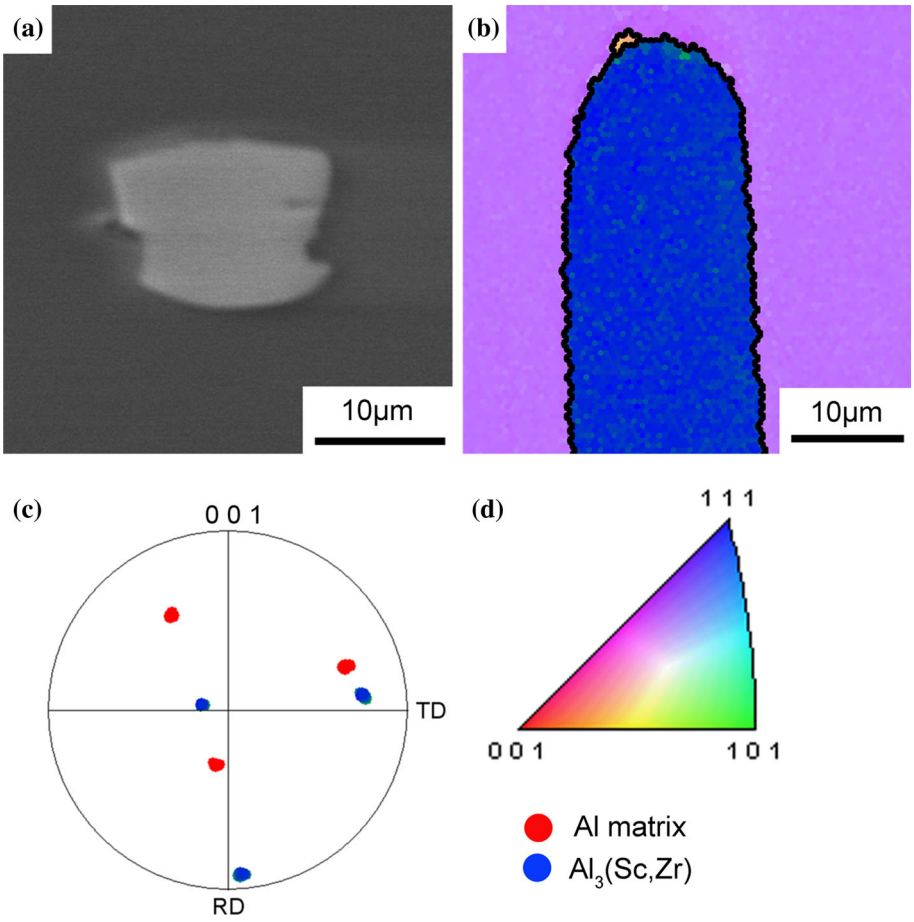

Fig. 7 SEM image (**a**), inverse pole figure from EBSD analysis (**b**) and the pole figure along (001) (**c**), and the *standard triangle* (**d**), of one $Al_3(Sc,Zr)$ particle in high purity Al-0.25Sc-0.25Zr alloy, respectively. The $Al_3(Sc,Zr)$ particle is located within the α-Al matrix

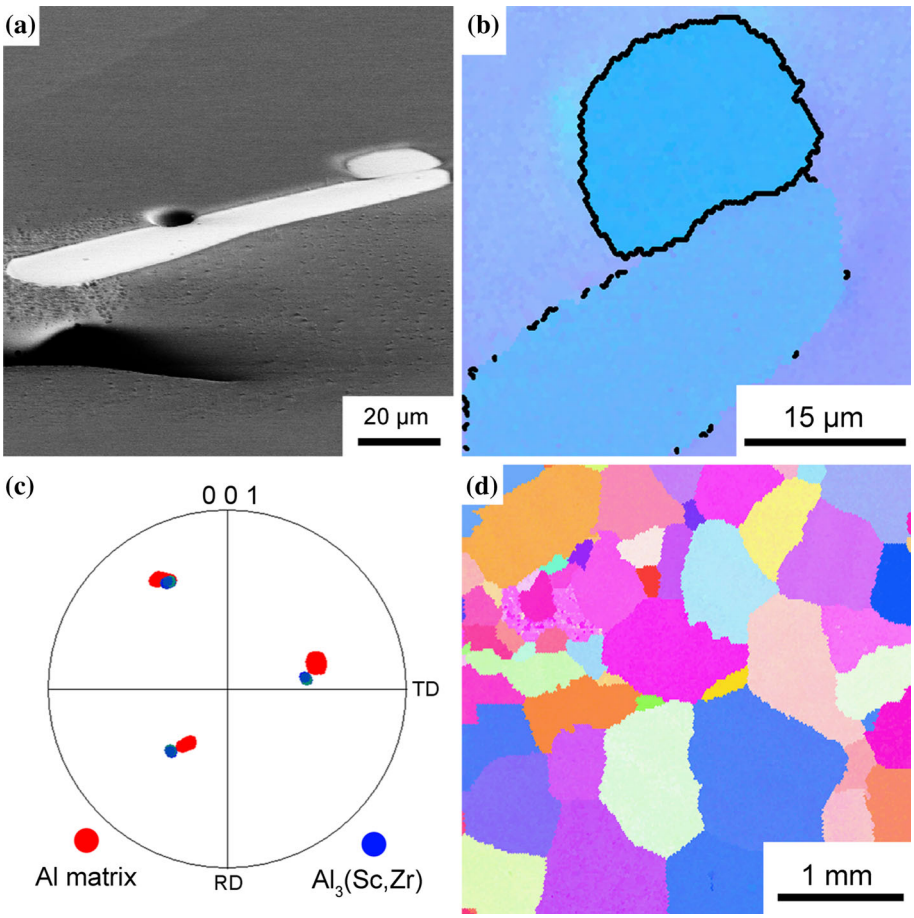

Fig. 8 SEM image (**a**), inverse pole figure from EBSD analysis (**b**) and the pole figures along (001) (**c**) of another $Al_3(Sc,Zr)$ particle in high purity Al-0.25Sc-0.25Zr alloy, respectively. EBSD mapping of a large area is also shown in (**d**)

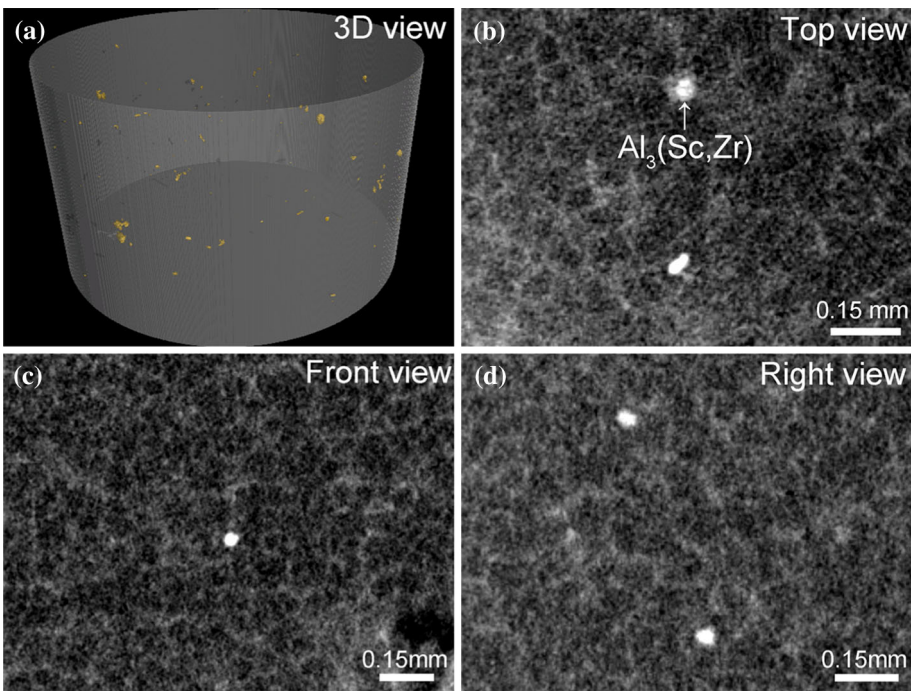

Fig. 9 Computer tomography 3-D scanning image (**a**), top side viewed image (**b**), front side viewed image (**c**), and rectangular to one front side viewed image (**d**) of high purity Al-0.25Sc-0.25Zr alloy, respectively

times less than to that of Zr (6.8 K/wt%, Table 2). It should be noted here that the comparison of the total growth restriction should be limited for the same purity level, e.g., high purity or commercial purity. It is not possible to compare high purity Al alloys with commercial purity Al alloys because the residual elements in commercial purity Al alloy result into an additional growth restriction. The total growth restriction in the case of a combined addition of Sc and Zr is smaller than that in the case of a single Zr addition. However, the grain size in the case of a combined addition of Sc and Zr (Fig. 4) is smaller than that in the case of a single Zr addition (Fig. 2), strongly indicating that an important interaction between Sc and Zr on heterogeneous nucleation may occur, and that heterogeneous nucleation dominates grain refinement. The possible interactions can be attributed to the fact that the combined addition of Zr and Sc reduces the solute solubility in the equilibrium of each other [17, 18] forcing the formation of further particles so that new nucleating sites are available for the nucleation of α-Al.

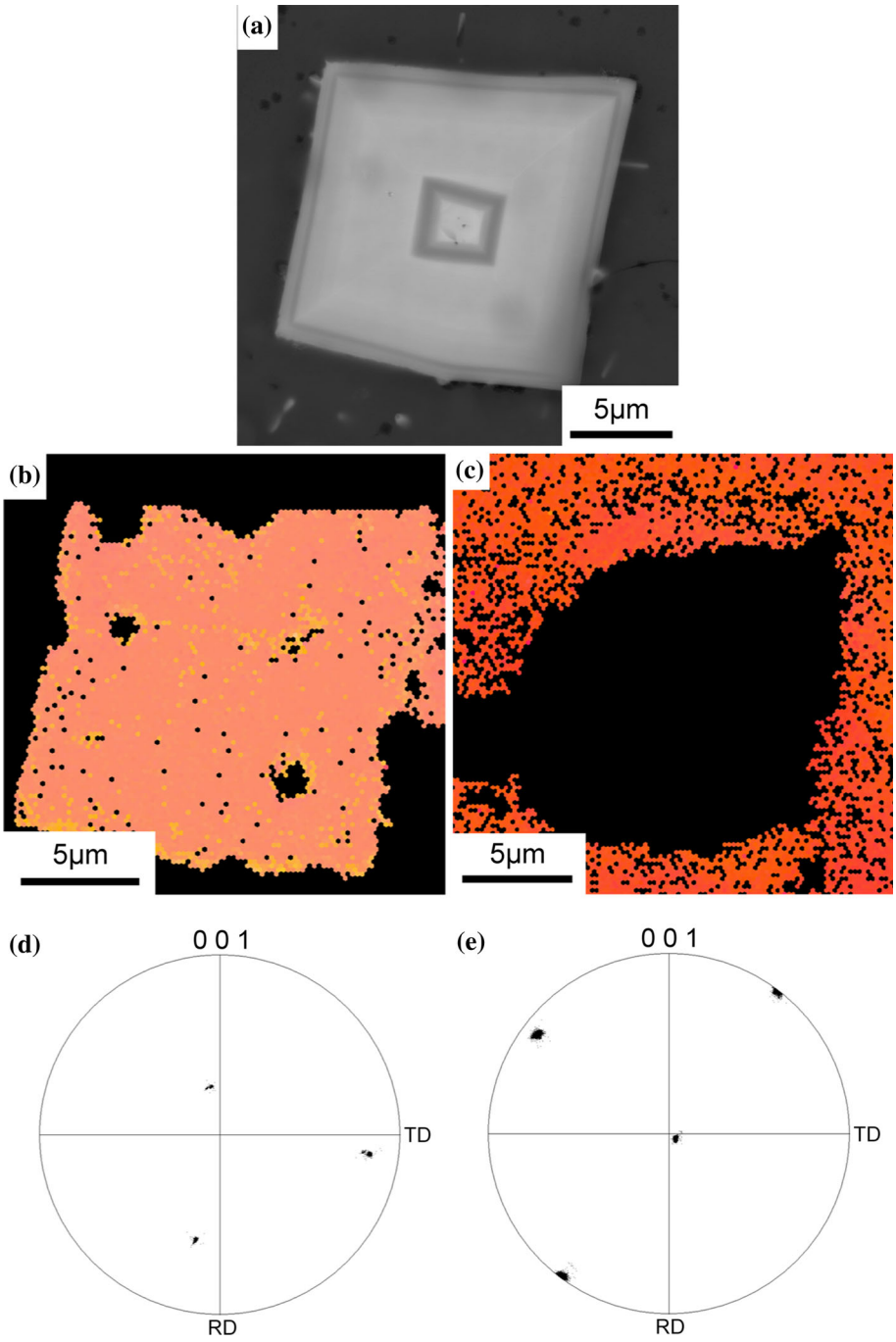

Fig. 10 SEM image (**a**), inverse pole figure from EBSD analyses and the pole figures along (001) of $Al_3(Sc,Zr)$ particle (**b**, **d**) and α-Al matrix (**c**, **e**) in commercial purity Al-0.25Sc-0.25Zr alloy, respectively. The $Al_3(Sc,Zr)$ particle is located within the α-Al matrix

Effects of solidification conditions on as-cast microstructure of high purity Al alloy with the additions of Sc and/or Zr

Solidification conditions have important effects on the nucleation and growth of Al alloys. Figure 5 shows the as-cast microstructure of high purity Al with Sc and/or Zr additions solidified at a lower cooling rate (20 °C/min) than that of the standard TP-1 method (4 °C/s). The single addition of Zr or Sc produces no significant grain refinement. Most grains appear to be columnar. Even with a combined addition of Zr and Sc, no significant grain refinement was observed except at the highest concentrations (0.25Zr and 0.25Sc, Fig. 5j), at which $Al_3(Sc,Zr)$ is pro-eutectic.

In contrast, a higher cooling rate (20 °C/s) leads to a significant grain refinement in the cases of a single or combined Zr and Sc addition, as shown in Fig. 6. The grain size appears to be largely independent on the Sc and/or Zr addition. This observation strongly indicates that a standard solidification condition (e.g., TP-1 test) has to be used when grain refinement is investigated. In the next sections, all samples for further microstructural characterisations are taken from the TP-1 test.

Primary $Al_3(Sc,Zr)$ in high purity Al alloy with the additions of Sc and Zr

Figure 7 shows one primary $Al_3(Sc,Zr)$ particle in high purity Al alloy with the addition of 0.25Sc and 0.25Zr. The primary $Al_3(Sc,Zr)$ particle is located within the α-Al matrix (Fig. 7b), which is believed to be engulfed during solidification. No low angle orientation relationship (e.g., cube to cube) was observed between the primary $Al_3(Sc,Zr)$ particle and the α-Al matrix, as shown in Fig. 7c, indicating that this pro-eutectic $Al_3(Sc,Zr)$ particle did not contribute to the heterogeneous nucleation and thereby grain refinement.

Figure 8 shows another primary $Al_3(Sc,Zr)$ particle in high purity Al alloy with the addition of 0.25Sc and 0.25Zr. The primary $Al_3(Sc,Zr)$ phase exhibits the same orientation with the α-Al matrix (Fig. 8b), as shown in Fig. 8c. Such

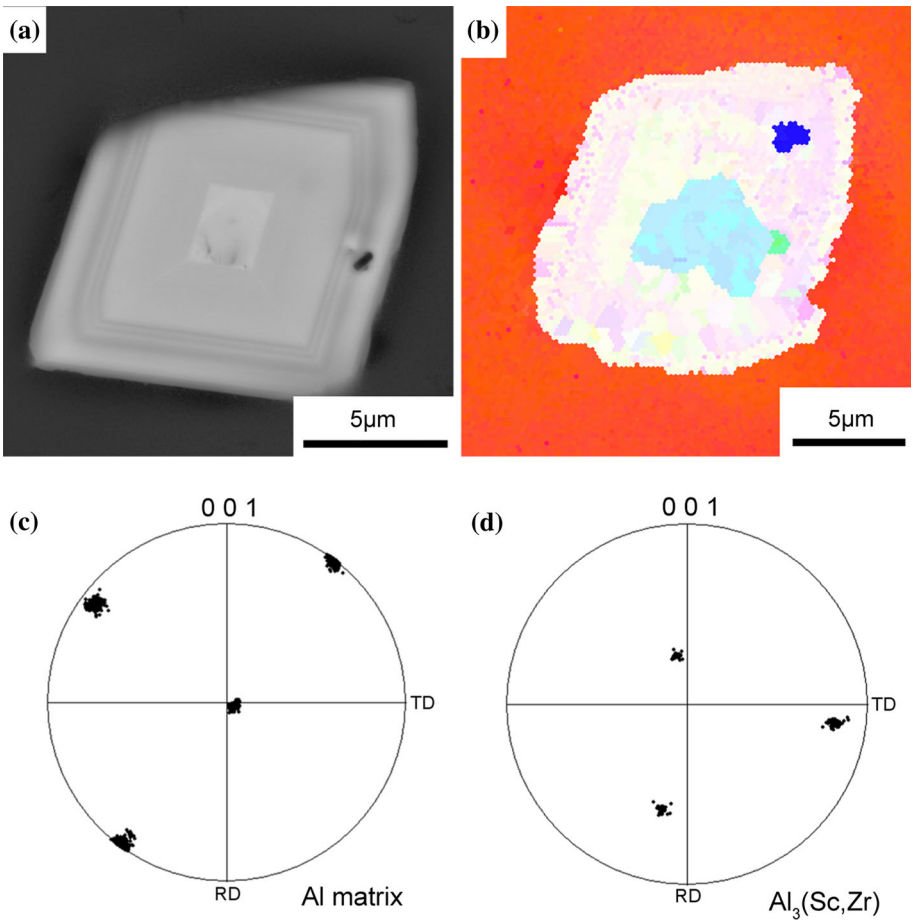

Fig. 11 SEM image (**a**), EBSD mapping (**b**) and the pole figures along (001) of α-Al matrix (**c**) and $Al_3(Sc,Zr)$ particle (**d**) in commercial purity Al-0.25Sc-0.25Zr alloy, respectively. The $Al_3(Sc,Zr)$ particle is located within the α-Al matrix

type of primary $Al_3(Sc,Zr)$ phases can be expected to contribute to the heterogeneous nucleation (Fig. 8d). This is also consistent with the free growth mode [2–6] that larger $Al_3(Sc,Zr)$ particles are more likely to be a potent nucleation site.

CT images of high purity Al alloy with the addition of 0.25Sc and 0.25Zr are shown in Fig. 9. In Fig. 9a, a 3-D image shows primary $Al_3(Sc,Zr)$ particles within the volume viewed. For clarity, frozen images of scans, viewed from top side (Fig. 9b), front side (Fig. 9c), and rectangular to one front side (Fig. 9d), are provided as a supplement. From the scanning images, most primary $Al_3(Sc,Zr)$ phases are located along the grain boundaries, which can be attributed to the particles to be pushed by the advancing solidification front. It is generally accepted that the possible nucleation sites should be located within the α-Al matrix and exhibit the same orientation with the α-Al matrix. Therefore, these primary $Al_3(Sc,Zr)$ phases did not contribute to the heterogeneous nucleation and thereby grain refinement of Al alloys. It is not possible by CT to detect the internal structure within the primary $Al_3(Sc,Zr)$ phase in high purity Al alloys.

Primary $Al_3(Sc,Zr)$ in commercial purity Al alloy with the additions of Sc and Zr

Figure 10 shows one primary $Al_3(Sc,Zr)$ particle in commercial purity Al alloy with the addition of 0.25Sc and 0.25Zr. The "star-like" primary $Al_3(Sc,Zr)$ particle was found to be located within the α-Al matrix. The orientation of the primary $Al_3(Sc,Zr)$ particle is identical to the orientation of the α-Al matrix, as shown in Fig. 10b,c. Such type of primary $Al_3(Sc,Zr)$ phase is believed to contribute to the heterogeneous nucleation during solidification. Furthermore, a very interesting observation is that the primary $Al_3(Sc,Zr)$ particle appears to grow layer by layer, as shown in Fig. 10a. Some layers with a weaker contrast were observed. The thickness of one layer is about 0.2–0.3 μm. These layers are believed to be enriched in impurities (e.g., Si, Fe, Cu, Mg, Ti), which are always present in commercial purity Al alloys (Table 1). The presence of the impurities causes a significant effect on nucleation and growth of the primary $Al_3(Sc,Zr)$ phase. Such type of primary $Al_3(Sc,Zr)$ phases contributes significantly to the heterogeneous nucleation and thereby

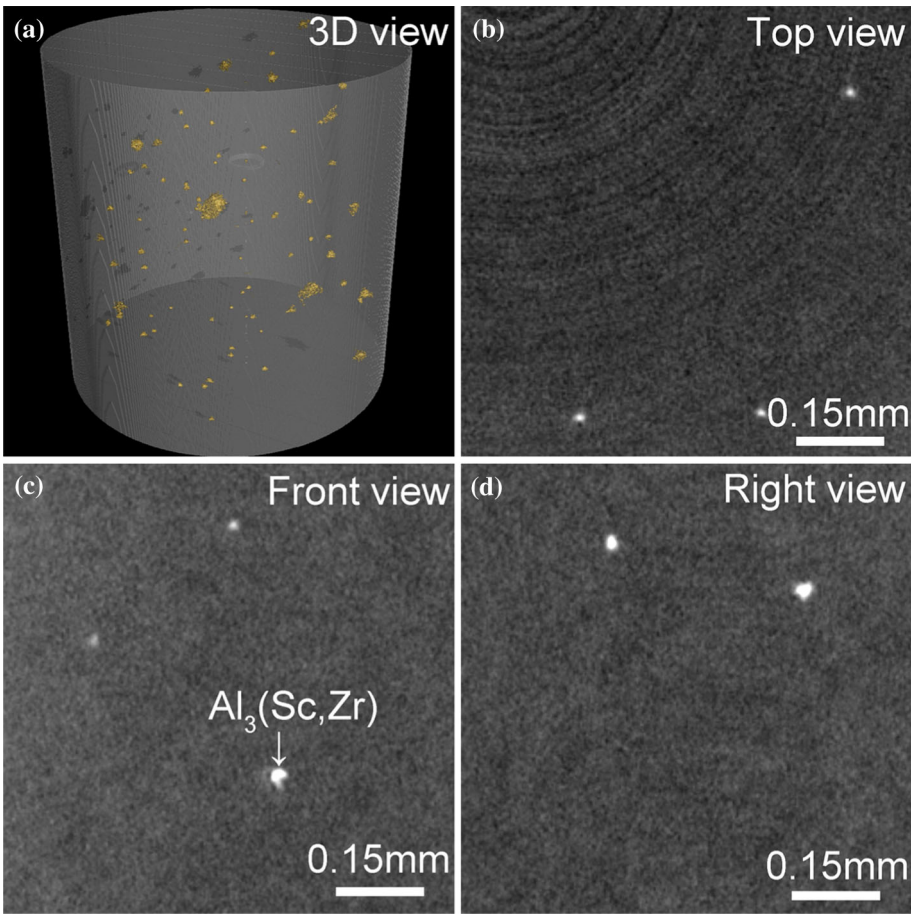

Fig. 12 Computer tomography 3-D scanning image (**a**), top side viewed image (**b**), front side viewed image (**c**), and rectangular to one front side viewed image (**d**) of commercial purity Al-0.25Sc-0.25Zr alloy, respectively

grain refinement of Al alloys. However, no significant enrichment of the impurities was measured using EDX in SEM, further high-resolution microstructure characterisation (i.e. TEM and atom probe tomography) is still required.

Figure 11 shows another primary Al_3(Sc,Zr) particle in commercial purity Al alloy with the addition of 0.25Sc and 0.25Zr. The primary Al_3(Sc,Zr) particle was found to be also located within the α-Al matrix. Within the Al_3(Sc,Zr) particle, a layered structure was observed again. In fact, the layered structure is typical for commercial purity Al alloys. EBSD analysis reveals that the primary Al_3(Sc,Zr) phase exhibits a considerable mismatch in orientation to the α-Al matrix. Such type of primary Al_3(Sc,Zr) phase did not contribute to the heterogeneous nucleation. It should be noted that, although the orientation relationship of the primary Al_3(Sc,Zr) phase does not remain the same with the α-Al matrix in commercial purity Al alloys, much more primary Al_3(Sc,Zr) phases are located within the α-Al matrix, when compared with high purity Al alloys. This observation can also be further supported using CT taken from commercial purity Al alloy with the addition of 0.25Sc and 0.25Zr, as shown in Fig. 12. From 3-D image (Fig. 12a), most primary Al_3(Sc,Zr) phases are located within the α-Al matrix, although the contrast of grain boundaries is not very clear.

In order to further enhance the contract, Fig. 13 shows primary Al_3(Sc,Zr) particles in a commercial Al-6Zn-2Mg alloy with 0.25Sc, 0.15Zr, and 0.01Ti additions. It should be noted here that the presence of 0.01Ti can be attributed to the used commercial purity Al, which contains about 0.0117 Ti (Table 1), as described in "Experimental material and procedures" section. It should also be noted here that the investigation of the commercial Al-6Zn-2Mg alloy with 0.25Sc, 0.15Zr, and 0.01Ti additions is mainly to elucidate the distribution of the primary Al_3(Sc,Zr) in commercial purity Al alloys because the nucleation and growth of primary Al_3(Sc,Zr) in commercial Al-6Zn-2Mg alloy with 0.25Sc, 0.15Zr and 0.01Ti additions is different from that in binary or ternary Al–Sc–Zr alloys (alloys 1–20). The enrichment of Zn and Mg along the grain boundaries makes it possible to determine the grain boundaries (brighter contrast than the α-Al matrix) and to elucidate the distribution of the primary Al_3(Sc,Zr). It is very clear that most primary Al_3(Sc,Zr) particles are indeed located within the α-Al matrix, which are responsible for

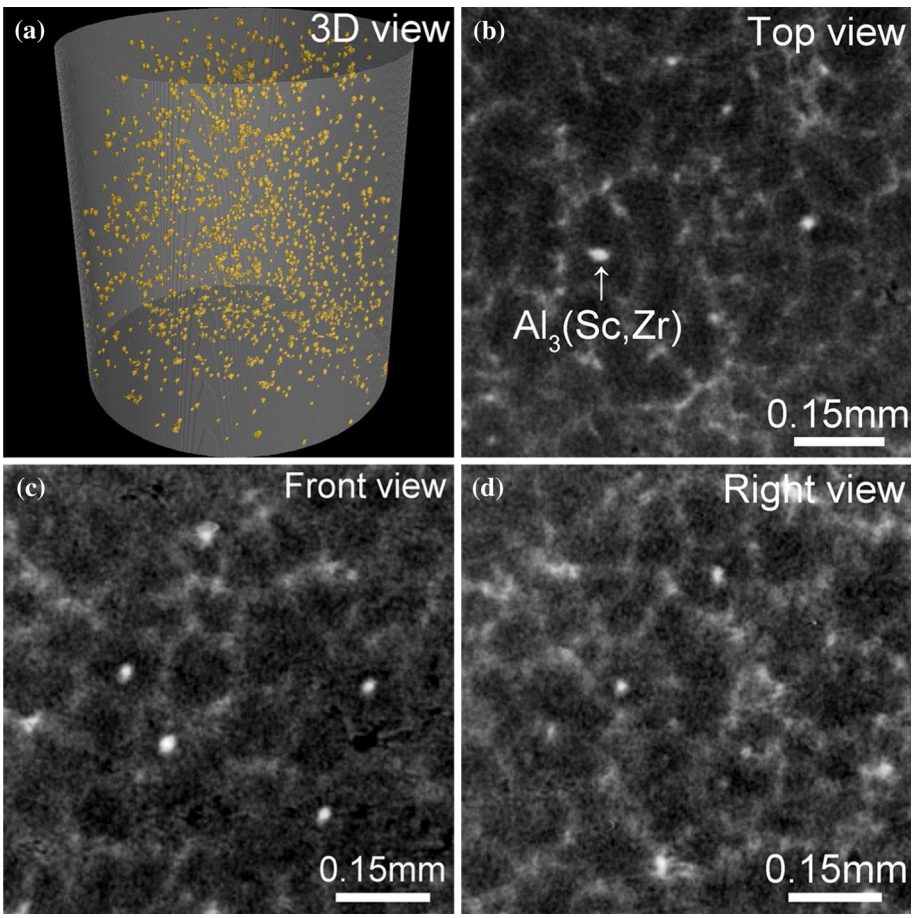

Fig. 13 Computer tomography 3-D scanning image (**a**), top side viewed image (**b**), front side viewed image (**c**), and rectangular to one front side viewed image (**d**) of commercial Al-6Zn-2Mg-0.25Sc-0.01Ti-0.15Zr alloy, respectively

heterogeneous nucleation of α-Al. Similar to Fig. 9, the movies, viewed from top side (Figs. 12b, 13b), front side (Figs. 12c, 13c), and rectangular to one front side (Figs. 12d, 13d), are also provided as a supplement.

Discussion

Impurity effect on the number density, size, and size distribution of primary $Al_3(Sc,Zr)$ phases

The final grain size of Al alloy is dependent on the number density, size, and size distribution of primary $Al_3(Sc,Zr)$ phases and the growth restriction of Al. The growth restriction of Al alloy is dependent on the cooling rate, liquid flow field and growth restriction factor of the alloying elements. In this study, the cooling rate, liquid flow field can be regarded to be identical because the standard TP-1 test was performed. As there is also little influence of growth restriction on Al caused by Zr, Sc addition and only low addition of other elements (Table 2), the factors affecting the final grain size is mainly by the number density, size, and size distribution of primary $Al_3(Sc,Zr)$ phases.

The number density, size and size distribution of primary $Al_3(Sc,Zr)$ phases itself is dependent on the impurity and the growth restriction on $Al_3(Sc,Zr)$ phase. The number density of primary $Al_3(Sc,Zr)$ phases in commercial purity Al-0.25Sc-0.25Zr alloy (Fig. 12a) was evaluated to be about 16.44 mm^{-3} from CT data analysis, which is higher than that (12.79 mm^{-3}) in high purity Al-0.25Sc-0.25Zr alloy (Fig. 9a), as shown in Fig. 14a. The presence of the alloying elements [e.g., Zn (6), Mg (2)] in commercial Al-6Zn-2Mg-0.25Sc-0.01Ti-0.15Zr alloy resulted into a significant increase of number density (259.08 mm^{-3}). However, as described above, the increase of number density cannot be directly related to the impurity effect because the alloying elements with high contents already changes the growth restriction and solidification behaviors.

Other important parameters (e.g., the size and the size distribution) were also determined, as shown in Fig. 14b–d, respectively. The mean primary $Al_3(Sc,Zr)$ particle size in commercial purity Al-0.25Sc-0.25Zr alloy is about 0.055 ± 0.044 mm, which is larger than that (0.0216 ± 0.034 mm) in high purity Al-0.25Sc-0.25Zr alloy and that (0.03889 ± 0.014 mm) in commercial Al-6Zn-2Mg-0.25Sc-0.1Ti-0.15Zr alloy. Furthermore, it should be noted that the standard deviation in commercial purity Al-0.25Sc-0.25Zr alloy is much smaller than that in high purity Al-0.25Sc-0.25Zr alloy, indicating that the size distribution of the primary $Al_3(Sc,Zr)$ particles in commercial purity Al-0.25Sc-0.25Zr alloy is much more

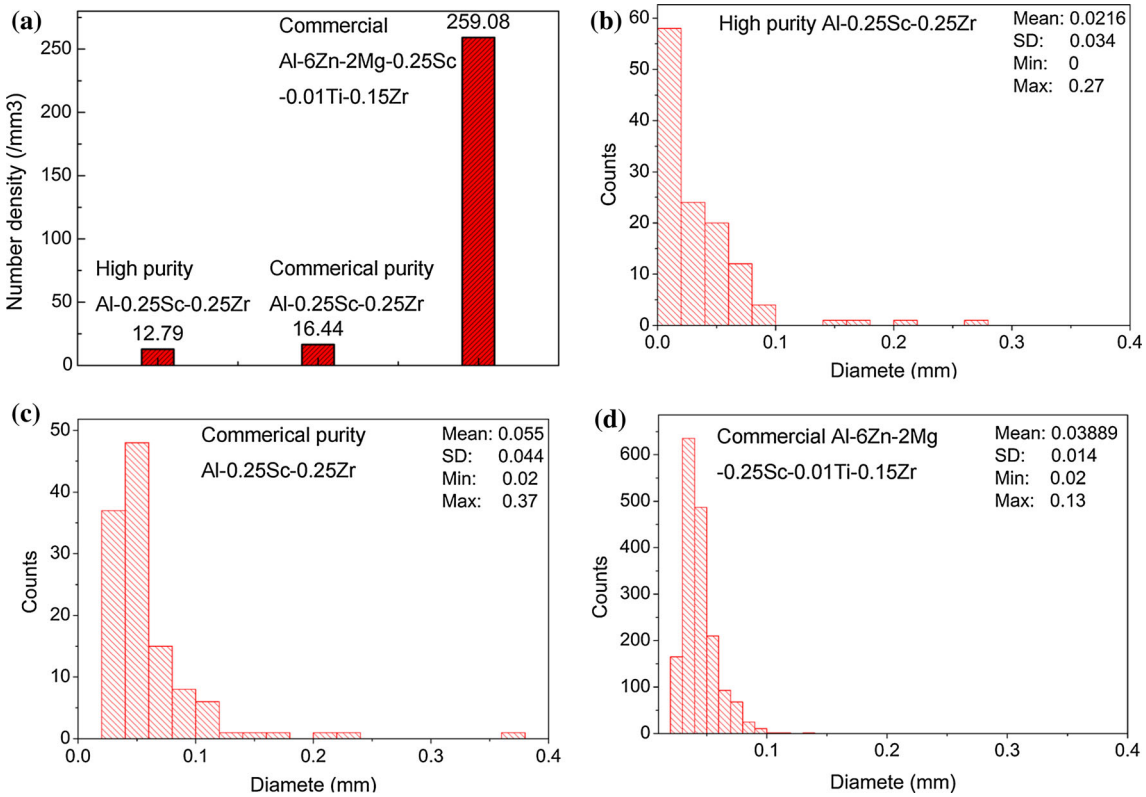

Fig. 14 Number density (**a**), and size distribution of $Al_3(Sc,Zr)$ particles in high purity Al-0.25Sc-0.25Zr alloy (**b**), commercial purity Al-0.25Sc-0.25Zr alloy (**c**), and commercial Al-6Zn-2Mg-0.25Sc-0.01Ti-0.15Zr alloy (**d**), respectively

narrow and uniform, and thus much more $Al_3(Sc,Zr)$ particles can be activated for a given undercooling interval. The standard deviation in commercial Al-6Zn-2Mg-0.25Sc-0.1Ti-0.15Zr alloy is even smaller than that in commercial purity Al-0.25Sc-0.25Zr alloy. However, this can be attributed to the alloying elements (e.g., Zn, Mg) with higher concentrations in the alloy. These analyses on the number density and the size, as well as the size distribution of primary $Al_3(Sc,Zr)$ phase can be used to interpret the observed grain size for Al.

Impurity effect on the nucleation and growth of primary $Al_3(Sc,Zr)$ phases

The presence of impurities [i.e., Si (0.0675), Fe (0.805), Cu (0.0011), Mg (0.0113), and Ti (0.0117), Table 1] in commercial purity Al-0.25Sc-0.25Zr alloy results into significant effects on the number density (Fig. 14a), size and size distribution of primary $Al_3(Sc,Zr)$ particles (Fig. 14b, c). Ti not only has a large growth restriction effect on Al but also on $Al_3(Sc,Zr)$. Ti was believed to partition easily into the nucleants, forming a Ti-rich region because of its strong partition behavior (k_{Ti}, 6.7 in pure Al [25]). The possible formation of Ti-rich layer has been reported to reduce the growth velocity of the nucleated $Al_3(Sc,Zr)$ particles and increase the maximum undercooling achievable before recalescence [11]. Thus, only small $Al_3(Sc,Zr)$ particles were observed, as shown in Figs. 10 and 11. The high growth restriction effect on $Al_3(Sc,Zr)$ allows more particles to be active in nucleation, and consequently increases the number density of the $Al_3(Sc,Zr)$ particles, subsequently acting as active nucleation sites for Al, finally giving rise to a fine Al grain size.

In order to further elucidate the nucleation and growth of primary $Al_3(Sc,Zr)$ particle, Fig. 15 shows a SEM image, line scan EDX analyses of primary $Al_3(Sc,Zr)$ particle in commercial Al-6Zn-2Mg-0.25Sc-0.01Ti-0.15Zr alloy. Five different sections are marked from the center to the edge of primary $Al_3(Sc,Zr)$ particle, as shown in Fig. 15a, c. From Fig. 15c, Sc, Zr, and Ti were observed to be enriched in the center of primary $Al_3(Sc,Zr)$ particle as the Zr concentration (0.15) is above the maximum solubility (0.11), which was marked as section I in Fig. 15a. Subsequently, a peritectic reaction layer (dark), as marked with section II in Fig. 15a, can be observed on the initial pro-peritectic $Al_3(Sc,Zr)$ particle. Interestingly, an enrichment or a segregation of impurities (e.g., Fe, Si, Cu, Mg, and Ti) induced by the phase transformation from peritectic to eutectic reaction was also observed, which was marked as section III in Fig. 15a.

The phase transformation from peritectic to eutectic reaction induced by impurities can be further supported

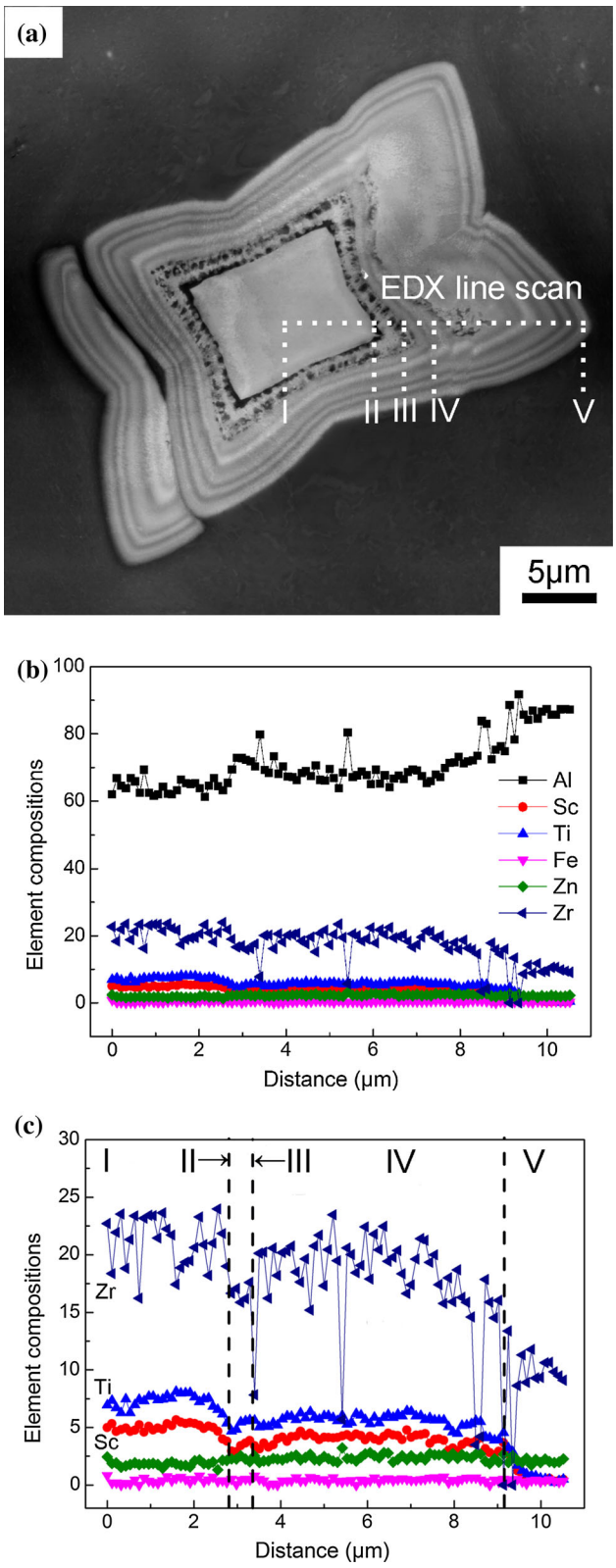

Fig. 15 SEM image (**a**), line scan EDX analyses (**b**, **c**) of primary $Al_3(Sc,Zr)$ particle in commercial Al-6Zn-2Mg-0.25Sc-0.01Ti-0.15Zr alloy. Five different areas from the center to the edge of $Al_3(Sc,Zr)$ particle are marked in (**a**) and correlated to (**c**)

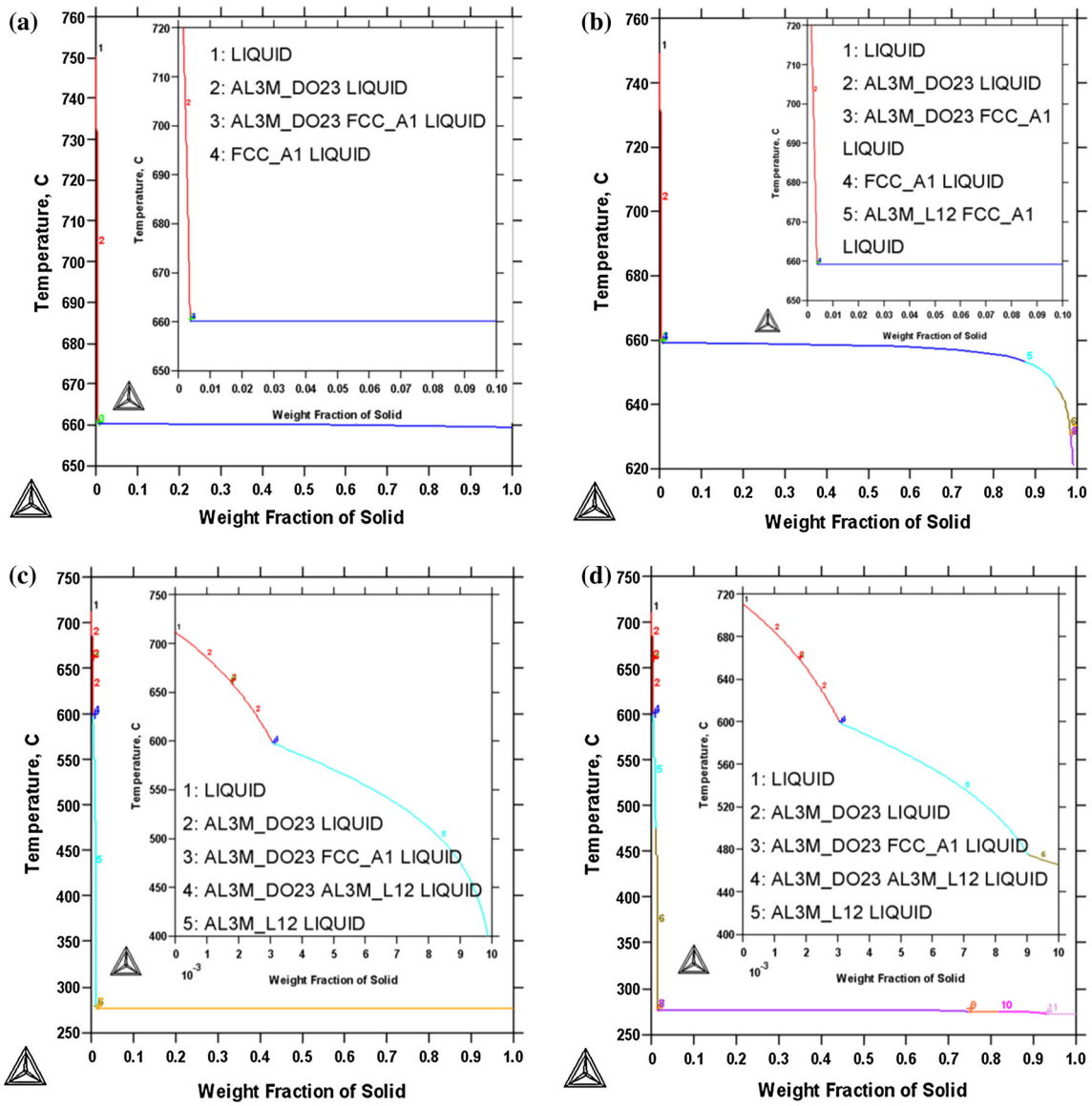

Fig. 16 ThermoCalc simulation of high purity Al-0.25Sc-0.25Zr alloy (**a**), commercial purity Al-0.25Sc-0.25Zr-0.1Fe-0.1Si alloy (**b**), high purity Al-0.25Sc-0.01Ti-0.15Zr alloy (**c**), and commercial purity Al-0.25Sc-0.01Ti-0.15Zr-0.1Fe-0.1Si alloy (**d**), respectively

using ThermoCalc simulation, as shown in Fig. 16. In high purity Al-0.25Sc-0.25Zr alloy, only the Al_3Zr phase is predicted, as shown in Fig. 16a, because the Zr concentration is higher than 0.11 and the Sc concentration is less than 0.55 (Table 2). With the presence of Fe (0.1) and Si (0.1), the formation of Al_3M_L12 ($Al_3(Sc,Zr)$) is predicted, as shown in Fig. 16b, strongly indicating that the mode of transformation changes from peritectic to eutectic because the Al_3M_L12 ($Al_3(Sc,Zr)$) phase is formed via an eutectic reaction. Similarly, with the presence of Ti (0.01), the formation of Al_3M_L12 ($Al_3(Sc,Zr)$) is also predicted even in high purity Al, as shown in Fig. 16c. In the case of the co-existence of Ti (0.01) and other impurities (e.g., 0.1 Fe, 0.1 Si), the formation of Al_3M_L12 ($Al_3(Sc,Zr)$) is also predicted (Fig. 16d). Clearly, the presence of the impurities (i.e., Fe, Si, Ti) induced the growth mode transition from peritectic to eutectic.

Interestingly, after the transition from peritectic to eutectic, the $Al_3(Sc,Zr)$ particle grows layer by layer by an divorced eutectic reaction, which was marked as section IV in Fig. 15a. It is well accepted that $Al_3(Sc,Zr)$ phase and Al cannot grow easily as a completed eutectic due to the small volume fraction of $Al_3(Sc,Zr)$ phase available. However, there is an excellent lattice match between $Al_3(Sc,Zr)$

Table 3 Lattice parameters and mismatch between Al_3Sc, Al_3Zr with Al matrix [25]

Particles	Lattice parameters (nm)	Mismatch (%)	Orientation relationship
Al_3Zr	DO_{23}	0.8	Any plane and directions
	$a = 0.4014$		
	$c = 0.433$		
	$L1_2$		
	$a = 0.405$		
Al_3Sc	$L1_2$	<1.5 (1.2)	Any plane and directions
	$a = 0.4105$		

phase and Al (Table 3). Therefore, an eutectic reaction is easily initiated at the interface of $Al_3(Sc,Zr)$ phase and Al to the liquid. Once the interface is covered, further nucleation of the $Al_3(Sc,Zr)$ phase is required to start the next eutectic reaction. As a result, subsequent layers of $Al_3(Sc,Zr)$ phase and Al resulting from a eutectic reaction can be observed in section IV in Fig. 15a. Note that the eutectic reaction is fundamentally different from the peritectic reaction in which the pro-peritectic phase is partly dissolved. Eventually, the layered growth obtains a size at which the critical size of $Al_3(Sc,Zr)$ phase is fulfilled for a given undercooling for Al according to the free growth model [2–6] and Al will grow freely, which was marked as section V in Fig. 15a. The successive large growth by eutectic reaction results into a narrow size distribution of $Al_3(Sc,Zr)$ particles on which free growth of Al can occur. In CT investigations, these layers are beyond the resolution of the CT methods used and the total composite particles are detected. It is these $Al_3(Sc,Zr)$ particles in a narrow size distribution, as shown in Figs. 12 and 13, that correspond to the onset of free grow [2–6] and the observed fine grain size of Al.

Over, this argument is fully consistent with (i) the free growth model [2–6], which suggests the size and size distribution of the nucleation sites are key factors affecting the nucleation and free growth of α-Al, (ii) the modified free growth model [7], which suggests the nucleation potency of inoculation particles is reduced by the solute field (impurities-rich region) that develops close to existing, growing equiaxed grains under near isothermal conditions. Solute suppressed nucleation leads to much lower nucleated grain densities, higher nucleation undercoolings and longer times to recalescence when further nucleation events are halted. In all cases, a solute-rich region is required for an enhanced grain refinement. The presence of impurities can enhance the formation of the solute-rich region. On the basis of above discussion, it can be concluded that heterogeneous nucleation is a dominant factor affecting the grain refinement.

Conclusions

In the case of high purity Al alloys, primary $Al_3(Sc,Zr)$ particles were pushed to grain boundaries by the moving solidification front. Such type of primary $Al_3(Sc,Zr)$ phase did not contribute to the heterogeneous nucleation, and thereby grain refinement of Al alloys. In the case of commercial purity Al alloy, the presence of impurities enhances the heterogeneous nucleation of primary $Al_3(Sc,Zr)$ phase. Primary $Al_3(Sc,Zr)$ phases are located within the α-Al matrix, and maintain the same orientation with the α-Al matrix. The presence of impurities also induces a transition on primary $Al_3(Sc,Zr)$ phase from a peritectic to eutectic reaction. In the case of commercial purity Al alloys, a transformation by subsequent eutectic reaction in front of a layer (Al) by layer ($Al_3(Sc,Zr)$) growth was observed, which led to a narrow size distribution. In contrast, in the case of high purity Al alloys, a featureless structure and no subsequent grain refinement of Al was observed. This investigation demonstrates that impurities have important effects on the nucleation and growth of primary $Al_3(Sc,Zr)$ phases and subsequently on Al in Al alloys. Controlling impurities and their concentrations can enhance the grain refinement of Al alloys. Moreover, a fine size and narrow size distribution of primary $Al_3(Sc,Zr)$ phases formed directly from liquid within the Al matrix may also facilitate a favorable condition for the homogenization and subsequent precipitation of secondary $Al_3(Sc,Zr)$ phase in the solid state.

Acknowledgement J. H. Li acknowledges C. Promer and A. Jahn for their help on etching the samples in Austrian Foundry Research Institute, S. Modritsch for her help on electro-polishing the samples at the Erich Schmidt Institute of Materials Science of the Austrian Academy of Science.

References

1. Easton MA, StJohn DH (1999) Grain refinement of aluminum alloys: part I. The nucleant and solute paradigms—a review of the literature. Metall Mater Trans A 30:1613–1623
2. Greer AL, Bunn AM, Tronche A, Evans PV, Bristow DJ (2000) Modelling of inoculation of metallic melts: application to grain refinement of aluminium by Al–Ti–B. Acta Mater 48:2823–2835
3. Quested TE, Greer AL (2004) The effect of the size distribution of inoculant particles on as-cast grain size in aluminium alloys. Acta Mater 52:3859–3868
4. Quested TE, Greer AL (2005) Grain refinement of Al alloys: mechanisms determining as-cast grain size in directional solidification. Acta Mater 53:4643–4653
5. Quested TE, Dinsdale AT, Greer AL (2005) Thermodynamic modelling of growth-restriction effects in aluminium alloys. Acta Mater 53:1323–1334
6. Quested TE, Greer AL (2005) Athermal heterogeneous nucleation of solidification. Acta Mater 53:2683–2692

7. Shu D, Sun BD, Mi J, Grant PS (2011) A quantitative study of solute diffusion field effects on heterogeneous nucleation and the grain size of alloys. Acta Mater 59:2135–2144
8. StJohn DH, Qian M, Easton MA, Cao P (2011) The interdependence theory: the relationship between grain formation and nucleant selection. Acta Mater 59:4907–4921
9. Men H, Fan Z (2011) Effects of solute content on grain refinement in an isothermal melt. Acta Mater 59:2704–2712
10. Iqbal N, van Dijk NH, Hansen T, Katgerman L, Kearley GJ (2004) The role of solute titanium and TiB_2 particles in the liquid–solid phase transformation of aluminum alloys. Mater Sci Eng A 386:20–26
11. Iqbal N, van Dijk NH, Offerman SE, Geerlofs N, Moret MP, Katgerman L, Kearley GJ (2006) In situ investigation of the crystallization kinetics and the mechanism of grain refinement in aluminum alloys. Mater Sci Eng A 416:18–32
12. Iqbal N, van Dijk NH, Offerman SE, Moret MP, Katgerman L, Kearley GJ (2005) Real-time observation of grain nucleation and growth during solidification of aluminium alloys. Acta Mater 53:2875–2880
13. Schumacher P, Greer AL (1994) Heterogeneously nucleated α-Al in amorphous aluminium alloys. Mater Sci Eng A 178:309–313
14. RØyset J, Ryum N (2005) Scandium in aluminium alloys. Int Mater Rev 50:19–44
15. Toropova LS, Eskin DG, Kharakterova ML, Dobatkina TV (1998) Advanced aluminium alloys containing scandium: structure and properties. Gordon and Breach Science, Amsterdam
16. Norman AF, Prangnell PB, Mcewen RS (1998) The solidification behaviour of dilute aluminium–scandium alloys. Acta Mater 46:5715–5732
17. Seidman DN, Marquis EA, Dunand DC (2002) Precipitation strengthening at ambient and elevated temperatures of heat-treatable Al(Sc) alloys. Acta Mater 50:4021–4035
18. Fuller CB, Seidman DN, Dunand DC (2003) Mechanical properties of Al(Sc, Zr) alloys at ambient and elevated temperatures. Acta Mater 51:4803–4814
19. Knipling KE, Seidman DN, Dunand DC (2011) Ambient- and high-temperature mechanical properties of isochronally aged Al-0.06Sc, Al-0.06Zr and Al-0.06Sc-0.06Zr (at.%) alloys. Acta Mater 59:943–954
20. Morrison CB, Seidman DN, Dunand DC (2011) Coarsening resistance at 400 °C of precipitation-strengthened Al–Zr–Sc–Er alloys. Acta Mater 59:7029–7042
21. Morrison CB, Seidman DN, Dunand DC (2012) Effect of Er additions on ambient and high-temperature strength of precipitation-strengthened Al–Zr–Sc–Si alloys. Acta Mater 60:3643–3654
22. Liu ZX, Li ZJ, Wang MX, Weng YG (2008) Effect of complex alloying of Sc, Zr and Ti on the microstructure and mechanical properties of Al–5 Mg alloys. Mater Sci Eng A 483–484:120–122
23. Dalen ME, Seidman DN, Dunand DC (2008) Creep- and coarsening properties of Al-0.06 at.% Sc-0.06 at.% Ti at 300–450 °C. Acta Mater 56:4369–4377
24. Vlach M, Stulíková I, Smola B, Žaludová N, Černá J (2010) Phase transformations in isochronally annealed mould-cast and cold-rolled Al–Sc–Zr-based alloy. J Alloys Compd 492:143–148
25. Brandes EA, Brook GB (1992) Smithells metals reference handbook, 7th edn. Butterworth-Heinemann, Oxford